




Research Article
10.65520/erciyesfen.1892532

Imprint:

Volume: 42(2)
Year: 2026
Page: 437-460

 Osman ÖZENCİ^a
 Kazım ERCAN^b
 Mehmet Akif DÜNDAR^c

^a Asst. Prof., Yozgat Bozok University, osman.ozenc@yobu.edu.tr
^b Res. Asst., Yozgat Bozok University, kazim.ercan@yobu.edu.tr
^c Asst. Prof., Yozgat Bozok University, mehmetakif.dundar@bozok.edu.tr

* Corresponding Author

Received: 2/20/2026
Accepted: 5/23/2026

Citation:

Osman ÖZENCİ, Kazım ERCAN, Mehmet Akif DÜNDAR (2026). A Comparative Assessment of Plane Stress Finite Elements for Stress Analysis in a Rectangular Plate with a Central Circular Hole under Uniaxial Tension. *Erciyes University Journal of Institute Of Science and Technology*, 42(2), 437-460.
<https://doi.org/10.65520/erciyesfen.1892532>

A Comparative Assessment of Plane Stress Finite Elements for Stress Analysis in a Rectangular Plate with a Central Circular Hole under Uniaxial Tension

Abstract

This study presents a comparative assessment of three various plane stress finite element formulations—CPS4, CPS4R, and CPS4I—implemented in ABAQUS for the prediction of maximum stress in a rectangular plate with a central circular hole subjected to uniaxial tension. Numerical results were benchmarked against the theoretical solution based on the gross-section stress concentration factor over hole diameter-to-width ratios up to 0.8. The primary objective was to quantify the influence of element formulations on maximum stress estimation with increasing hole diameter-to-width ratio. Numerical results suggested that all element types successfully captured the progressive increase in maximum stress with increasing hole size. Nevertheless, systematic differences in accuracy were observed. The CPS4 element produced slight overestimations, whereas CPS4R consistently underestimated the reference solution, with discrepancies becoming more noticeable at higher geometric ratios where stress gradients are more pronounced. Among the examined formulations, CPS4I exhibited the most consistent and accurate agreement with the theoretical results, maintaining small and stable error levels across the entire investigated range. This was attributed to its incompatible mode enhancement that provides improved strain field representation, enabling more reliable resolution of localized stress peaks. The findings underscored the critical role of element formulation in ABAQUS for achieving accurate maximum stress predictions in perforated structural components subjected to uniaxial tensile loading.

Keywords: Stress concentration, Finite element analysis (FEA), Plane stress elements, Element formulation accuracy, Uniaxial tension, Finite-width perforated plates.



Tek Eksen Çekmede Merkezi Dairesel Delikli Dikdörtgen Bir Plakada Gerilme Analizi için Düzlem Gerilme Sonlu Elemanlarının Karşılaştırmalı Değerlendirmesi

Öz

Bu çalışma, tek eksenli çekme yüküne maruz bırakılmış, ortasında dairesel delik bulunan dikdörtgen bir plakanın maksimum gerilmesinin tahmini için ABAQUS'te uygulanan üç farklı düzlem gerilme sonlu eleman formülasyonunun—CPS4, CPS4R ve CPS4I—karşılaştırmalı bir değerlendirmesini sunmaktadır. Sayısal sonuçlar, delik çapının plaka genişliğine oranının 0.8'e kadar olan değerleri için, brüt kesit gerilme yığılma katsayısına dayanan teorik çözümle karşılaştırılmıştır. Çalışmanın temel amacı, delik çapı/genişlik oranının artmasıyla birlikte eleman formülasyonlarının maksimum gerilme tahmini üzerindeki etkisini nicel olarak belirlemektir.

Screened by
 iThenticate®
for Authors & Researchers



Except where otherwise noted, content in this article is licensed under a Creative Commons 4.0 International license. Icons by Font Awesome.

Sayısal sonuçlar, tüm eleman tiplerinin delik boyutu arttıkça maksimum gerilmedeki kademeli artışı başarıyla yakaladığını göstermiştir. Bununla birlikte, doğruluk açısından sistematik farklılıklar gözlemlenmiştir. CPS4 elemanı referans çözüme kıyasla hafif fazla tahminler üretirken, CPS4R elemanı özellikle gerilme gradientlerinin daha belirgin olduğu yüksek geometrik oranlarda referans çözümü tutarlı biçimde düşük tahmin etmiştir. İncelenen formülasyonlar arasında CPS4I elemanı, teorik sonuçlarla en tutarlı ve en doğru uyumu göstermiş; incelenen tüm oran aralığında küçük ve kararlı hata seviyelerini korumuştur. Bu durum, daha gelişmiş bir şekil değiştirme alanı temsili sağlayan ve yerel gerilme tepe değerlerinin daha güvenilir biçimde çözülmesine olanak tanıyan uyumsuz mod iyileştirmesine bağlanmıştır. Elde edilen bulgular, tek eksenli çekme yüküne maruz perforasyonlu yapısal bileşenlerde maksimum gerilme tahminlerinin doğruluğunu sağlamak açısından ABAQUS'te eleman formülasyonu seçiminin kritik önem taşıdığını vurgulamıştır.

Anahtar kelimeler: Gerilme yığılması, Sonlu elemanlar analizi (SEA), Düzlem gerilme elemanları, Eleman formülasyonu doğruluğu, Tek eksenli çekme, Sonlu genişlikte delikli plakalar.



1. Introduction

Geometric discontinuities such as holes, notches, and abrupt changes in cross-sectional geometry are inherent features of many engineering components [1–3]. These discontinuities disturb the uniform transmission of stresses, giving rise to localized stress amplification commonly referred to as stress concentration [3–5]. Such localized stress elevations frequently govern the onset of plastic deformation, fatigue crack initiation, and ultimate structural failure [4]. Consequently, the accurate characterization of stress fields in the vicinity of geometric discontinuities remains a central problem in solid mechanics and structural design [4,6,7]. Classical design handbooks, most notably Roark's Formulas for Stress and Strain, emphasize that localized peak stresses, rather than nominal stresses, often control failure mechanisms and must therefore be explicitly accounted for in mechanical design [8]. Among canonical elasticity problems, the rectangular plate containing a central circular hole and subjected to uniaxial tension has long served as a benchmark configuration due to its analytical tractability and engineering relevance. The earliest analytical solution to this problem was provided by Kirsch [9], who derived the exact stress field for an infinite elastic plate with a circular hole under uniform remote tension. This solution demonstrated that the maximum circumferential stress at the hole boundary reaches three times the nominal far-field stress, thereby establishing a fundamental result in the theory of stress concentration. Subsequent investigations extended these formulations to finite-width plates, anisotropic materials, and complex loading conditions, revealing that boundary proximity and finite geometry effects significantly influence both the magnitude and spatial distribution of stresses [10–12]. As a result, the classical infinite-domain assumption is often insufficient for practical engineering configurations, motivating the adoption of numerical approaches.

In this context, the finite element method (FEM) has become the dominant computational tool for analyzing stress fields in components containing geometric discontinuities [13–15]. FEM offers considerable flexibility in modeling complex geometries, realistic boundary conditions, and nonlinear material behavior [16,17]. However, accurately resolving steep stress gradients near discontinuities remains a persistent challenge [3]. The reliability of FEM predictions in such regions is strongly influenced by the choice of element formulation, interpolation order, numerical integration scheme, and mesh refinement strategy [18,19]. Inadequate element formulations may lead to artificial stiffening, spurious oscillations, or excessive numerical smoothing, thereby compromising the accuracy of peak stress predictions [20].

Commercial finite element software packages such as Abaqus provide a wide range of plane stress element formulations for two-dimensional elasticity analyses [21]. Among these, the fully integrated bilinear quadrilateral element (CPS4) [22], the reduced integration variant (CPS4R) [23], and the incompatible mode element (CPS4I) [24,25] are widely employed in engineering practice. Each of these formulations exhibits distinct numerical characteristics. Fully integrated elements are generally robust but may suffer from locking phenomena in bending-dominated problems [26]. Reduced integration elements mitigate locking and offer improved computational efficiency, yet they

may exhibit zero-energy modes and reduced stress accuracy. Incompatible mode elements enrich the displacement field locally, enabling improved representation of bending behavior and stress gradients, albeit at the cost of increased formulation complexity [27,28].

Despite their widespread use, the relative performance of these plane stress elements in capturing stress concentration effects has not been systematically quantified. Most existing studies on perforated plates emphasize the evaluation of stress concentration factors, geometric parametric effects, or experimental validation of numerical predictions [29,30]. However, the influence of the underlying finite element formulation itself is often treated implicitly. In particular, the comparative ability of commonly used plane stress elements to resolve the severe stress gradients near hole boundaries remains insufficiently explored. This gap is of practical significance, as engineers frequently rely on default element choices without detailed awareness of their limitations in stress-critical regions.

Unlike the majority of existing studies, which primarily focus on the evaluation of stress concentration factors or the influence of geometric parameters, the present work isolates and rigorously examines the role of the finite element formulation itself as a governing source of variability in stress predictions. In this regard, the study shifts the conventional focus from geometry-driven analysis to formulation-driven accuracy, thereby addressing a critical yet underexplored aspect of finite element modeling. In particular, this study introduces a systematic and quantitative comparison framework that evaluates the performance of commonly used plane stress elements not only in terms of peak stress estimation but also with respect to their ability to resolve steep stress gradients, accurately capture the spatial distribution of stresses, and demonstrate consistent mesh convergence behavior. By employing identical geometric configurations, loading conditions, and discretization strategies, the influence of element formulation is explicitly decoupled from other modeling parameters, thereby enabling an unbiased and physically meaningful assessment that is largely absent in the current literature. This controlled comparison framework ensures that the observed differences can be directly attributed to the intrinsic numerical characteristics of the elements, rather than external modeling choices, which significantly enhances the scientific rigor of the study. Furthermore, detailed insights into the numerical behavior of each element type in stress-critical regions are provided, highlighting their respective limitations and capabilities in a manner directly relevant to engineering applications. Such insights extend beyond conventional result reporting by offering a mechanistic understanding of element performance, particularly in regions dominated by high stress gradients. This formulation-centric perspective constitutes a distinct contribution by bridging the gap between theoretical element characteristics and their practical implications in stress concentration analysis, ultimately offering actionable guidance for the reliable selection of finite element types in design-oriented contexts. Consequently, the study not only complements existing SCF-based investigations but also provides a refined methodological basis for improving the accuracy and reliability of finite element analyses in engineering practice.

Motivated by these considerations, the present study conducts a systematic comparative assessment of CPS4, CPS4R, and CPS4I plane stress elements in Abaqus for modeling the stress field of a rectangular plate with a central circular hole under uniaxial tension. The emphasis is placed on their ability to accurately capture stress distributions, resolve stress concentration zones, and predict peak circumferential stresses along the hole boundary. Particular attention is devoted to mesh convergence behavior, numerical stability, and sensitivity to discretization. By establishing a clear and quantitative comparison, this work aims to provide practical guidance for element selection in stress concentration analyses and to enhance the reliability of finite element-based design practices.

2. Theory

Structural components containing geometric discontinuities, such as holes, are susceptible to localized stress amplification when subjected to external loading. This behavior is illustrated in Figure 1, which presents a finite-width rectangular plate with a central circular hole under uniaxial tensile stress σ . As shown in Figure 1(a), the presence of the hole disturbs the uniform stress field that would otherwise exist in an unperforated plate [31]. This disturbance leads to a non-uniform stress

distribution with a pronounced stress peak at the hole boundary, as schematically depicted in Figure 1(b).

To quantify this amplification, the stress concentration factor based on the gross cross-sectional area, K_{tg} , is defined as [31].

$$K_{tg} = \frac{\sigma_{max}}{\sigma} \quad (1)$$

where σ_{max} is the maximum stress occurring at the edge of the hole, and σ is the nominal stress calculated on the gross cross section, sufficiently far from the hole. The magnitude of K_{tg} depends on the geometric proportions of the plate and the applied loading condition [29].

Note that the stress concentration factor K_{tg} incorporates two distinct contributing mechanisms [31]:

(i) The increase in nominal stress associated with the reduction of the effective load-carrying area.

(ii) The additional stress amplification arising from the presence of a geometric discontinuity.

Thus, the stress concentration factor K_{tg} for a finite-width rectangular plate with a central single circular hole under uniaxial tension can be defined as follows [31]:

$$K_{tg} = 0.284 + \frac{2}{1 - \frac{d}{w}} - 0.6 \left(1 - \frac{d}{w}\right) + 1.32 \left(1 - \frac{d}{w}\right)^2 \quad (2)$$

Herein, d is the diameter of the circular hole, and w represents the width of the rectangular plate.

Eq. (2) expresses the stress concentration factor K_{tg} as a function of the hole-to-width ratio d/w . It is evident from this formulation that K_{tg} increases rapidly as the rectangular plate becomes narrower, that is, as the hole size approaches the plate width. In the limiting case where $d/w \rightarrow 1$, the remaining load-carrying ligament vanishes, and the stress concentration factor tends toward infinity ($K_{tg} \rightarrow \infty$), reflecting the loss of effective load transfer capacity in the plate.

Thus, the maximum stress at the edge of the hole, as illustrated in Figure 1(b), can be determined by multiplying the stress on the gross cross-section far from the hole σ by the corresponding stress concentration factor K_{tg} , as given below [31].

$$\sigma_{max} = K_{tg} \cdot \sigma \quad (3)$$

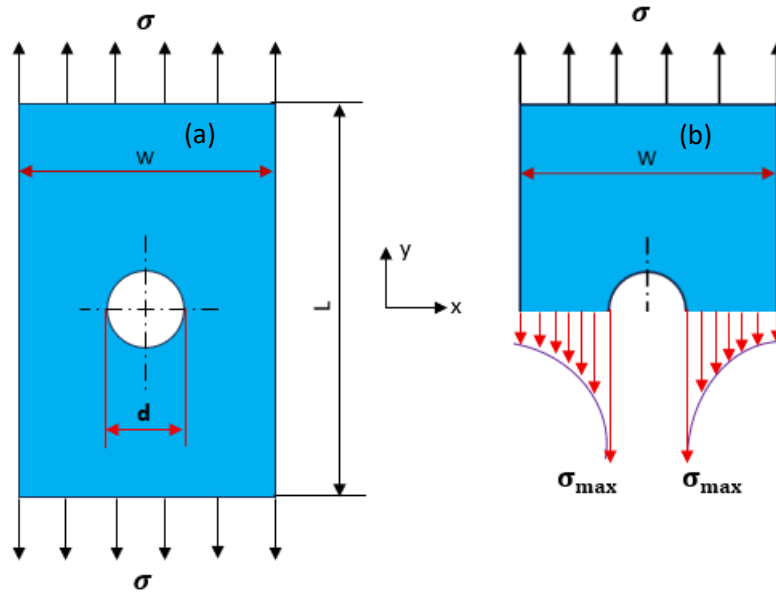


Figure 1. (a) Geometry and loading of a finite-width rectangular plate with a central circular hole under uniaxial tensile stress σ , (b) Schematic stress distribution near the hole [31].

In addition to the stress concentration factor based on the gross cross-sectional area K_{tg} , an alternative definition is provided through the stress concentration factor K_{tn} , which is referenced to the net cross-sectional area. For a two-dimensional finite-width rectangular plate with a single circular hole (Figure 1), K_{tn} can be defined as given below [31].

$$K_{tn} = \frac{\sigma_{max}}{\sigma_n} \quad (4)$$

Here, σ_n represents the net (nominal) stress and is described as follows [31]:

$$\sigma_n = \frac{\sigma}{\left(1 - \frac{d}{w}\right)} \quad (5)$$

Unlike K_{tg} , which reflects both the reduction in load-carrying area and the geometric disturbance of the stress field, K_{tn} accounts solely for stress amplification due to geometry. Consequently, as the plate becomes narrower and $d/w \rightarrow 1$, K_{tn} approaches unity, corresponding to a uniform tension member. This formulation provides an alternative means of evaluating the maximum stress and is particularly useful when stress gradients near the hole are of interest [4,29,31].

The correlation between K_{tg} and K_{tn} can also be defined as given below [31].

$$K_{tn} = K_{tg} \left(1 - \frac{d}{w}\right) = K_{tg} \left(\frac{\sigma}{\sigma_n}\right) \quad (6)$$

The above expression Eq. (6) clearly shows that K_{tg} incorporates both the stress amplification due to the reduction in effective load-carrying area and the geometric disturbance of the stress field, whereas K_{tn} isolates the geometric contribution alone. As the hole size increases relative to the plate width, the distinction between these two effects becomes increasingly significant, particularly when assessing stress gradients and local failure mechanisms.

For completeness, the stress concentration factor based on the net cross-sectional stress, K_{tn} , for a finite-width rectangular plate with a central circular hole under uniaxial tension (Figure 1) can be expressed explicitly as a function of the geometric ratio d/w . An empirical closed-form approximation commonly adopted in the literature is given by [31]

$$K_{tn} = 2 + 0.284 \left(1 - \frac{d}{w}\right) - 0.6 \left(1 - \frac{d}{w}\right)^2 + 1.32 \left(1 - \frac{d}{w}\right)^3 \quad (7)$$

Accordingly, the maximum stress at the edge of the hole, as depicted in Figure 1(b), can also be determined by accounting for the net-section-based stress concentration factor K_{tn} , as expressed below.

$$\sigma_{max} = K_{tn} \frac{\sigma}{\left(1 - \frac{d}{w}\right)} \quad (8)$$

Hence, the maximum stress at the edge of the hole can be evaluated using two equivalent formulations, depending on the choice of reference stress. When the stress on the gross cross-section far from the hole is used, the peak stress is obtained by multiplying this stress by the stress concentration factor K_{tg} , as expressed in Eq. (3). Alternatively, if the net cross-sectional stress is taken as the reference, the maximum stress may be determined using the factor K_{tn} , as given in Eq. (8). Although the reference stresses differ, both formulations describe the same physical stress amplification at the hole boundary and therefore provide consistent predictions of σ_{max} .

The curves presented in Figure 2 were generated using Eq. (2) and Eq. (7) to evaluate the stress concentration factors K_{tg} and K_{tn} , respectively, for hole diameter-to-width ratios up to $d/w = 0.8$. This upper limit was selected because the analytical expressions employed are derived based on geometric assumptions that become invalid as the hole size approaches the plate width. For $d/w > 0.8$ the remaining ligament is significantly reduced, resulting in pronounced stress gradients and strong boundary interactions that invalidate the concept of a well-defined gross and net section [31,32]. Under these conditions, the stress field can no longer be accurately captured by closed-form solutions, and the stress concentration factor increases rapidly toward infinity. Therefore, for larger hole sizes, a reliable assessment necessitates the use of numerical approaches, such as finite element analysis, rather than analytical formulations.

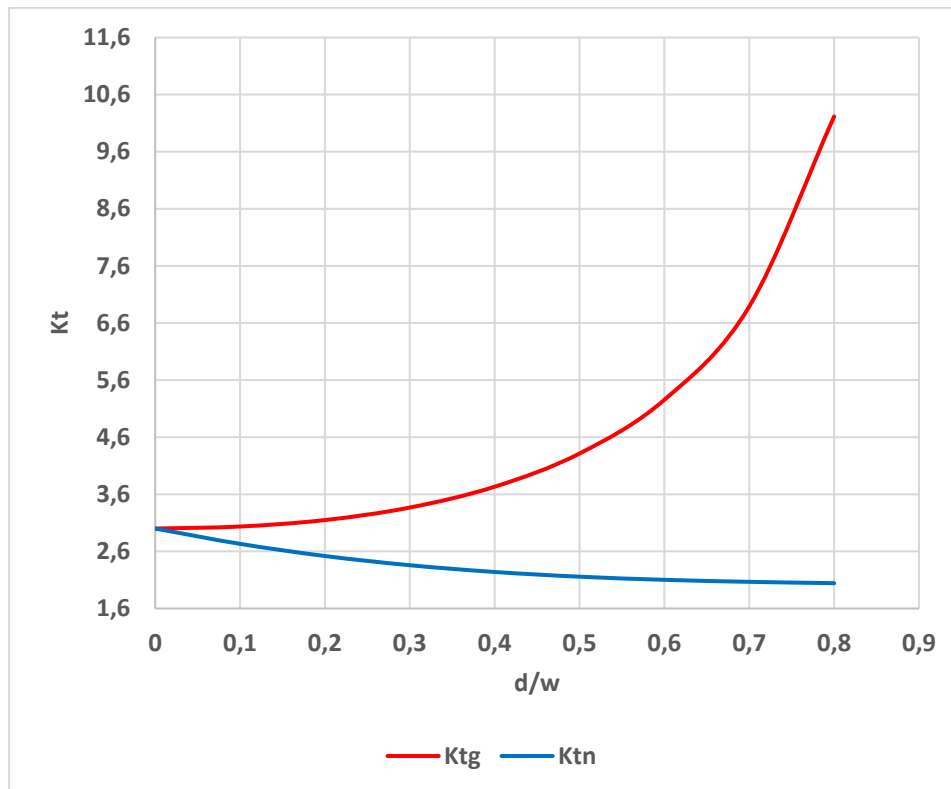


Figure 2. Stress concentration factors K_{tg} and K_{tn} for a finite-width thin plate with a circular hole subjected to uniaxial tension.

If a further clarification is needed, it should be noted that the empirical expressions used in Equations (2) and (7) for the stress concentration factors, K_{tg} and K_{tn} , are based on the classical results compiled by Peterson [31]. These expressions are valid within the range $d/w \leq 0.8$. For example, in Eq. (2), $K_{tg} = 0.284 + \frac{2}{1-\frac{d}{w}} - 0.6 \left(1 - \frac{d}{w}\right) + 1.32 \left(1 - \frac{d}{w}\right)^2$, the term $\frac{2}{1-\frac{d}{w}}$ approaches infinity as $d/w \rightarrow 1$, which is non-physical. Similarly, in Eq. (7), $K_{tn} = 2 + 0.284 \left(1 - \frac{d}{w}\right) - 0.6 \left(1 - \frac{d}{w}\right)^2 + 1.32 \left(1 - \frac{d}{w}\right)^3$, higher-order terms dominate for large d/w , producing unrealistic stress amplification. Therefore, these expressions should not be used beyond $d/w = 0.8$, as their predictions become unreliable and deviate from the physical behavior of plates with large holes. All comparisons in the present study respect this established validity range [31].

3. Finite Element Analysis

3.1. Finite Element Modeling Procedure

Finite element analyses were performed using Abaqus/Standard 2D [21] within a two-dimensional framework to investigate the stress distribution and stress concentration behavior of a finite-width plate with a central circular hole subjected to uniaxial tension. The geometric dimensions and material properties adopted in the numerical simulations are summarized in Table 1. The plate material was modeled as linear elastic and isotropic, representing ASTM A36 steel, with an elastic modulus of 200000 MPa and a Poisson's ratio of 0.3 [33]. A plane stress formulation was adopted to represent the thin-plate behavior. The plate was discretized using plane stress continuum elements, including CPS4, CPS4R, and CPS4I element types [28], to assess the influence of element formulation and integration scheme on the predicted stress concentration response. Geometric nonlinearity was incorporated by activating the NLGEOM option, enabling the numerical model to capture large-deformation effects associated with stress redistribution around the geometric discontinuity. Although the material behavior in this study is linear elastic and stress levels are moderate, geometric

nonlinearity (NLGEOM) was activated in the finite element model to account for potential local deformations, particularly near stress concentration regions such as the circular hole. As recommended [21], activating NLGEOM ensures that the stiffness matrix accounts for changes in geometry during loading, which can influence stress distributions even when global deformations are relatively small. This consideration is particularly relevant in problems involving stress concentrations, where localized deformation patterns may introduce second-order geometric effects that are not captured under a purely linear geometric assumption. This precaution guarantees that the numerical predictions remain accurate in regions where local bending or stress gradients may induce minor geometric effects, without significantly increasing computational cost. Moreover, the inclusion of NLGEOM provides a more general and robust formulation, ensuring that the solution remains valid even in the presence of subtle nonlinear geometric responses that may arise at higher stress levels or in refined mesh regions. In practice, the convergence study confirmed that including geometric nonlinearity did not alter the global stress results; however, it enhances the fidelity of the local stress field representation and eliminates any potential bias associated with geometric linearization [34].

A uniform uniaxial tensile stress of $\sigma = 100$ MPa (Table 1) was applied to define the far-field loading condition, providing a consistent elastic reference stress for evaluating stress concentration effects. The plate length-to-width ratio was selected as $L/w = 3$ to minimize boundary influences arising from the applied loading and constraints [34]. This ratio is widely adopted in stress concentration analyses to promote the development of a nearly uniform stress field away from the hole, ensuring that the stress amplification at the hole boundary is governed primarily by geometric discontinuity rather than end effects [34]. This selection is further supported by established findings in the literature [34], which demonstrate that the stress concentration factor (SCF) decreases rapidly with increasing L/w and approaches an asymptotic, nearly constant value for $L/w \geq 3$, regardless of the hole diameter-to-width ratio (d/w). This behavior indicates that, beyond this threshold, the influence of plate boundaries on the stress distribution in the vicinity of the hole becomes negligible. Therefore, the chosen ratio ensures the development of a sufficiently uniform far-field stress state, such that the stress concentration at the hole boundary is governed primarily by the geometric discontinuity rather than finite plate dimensions [34].

Table 1. Geometric specifications and material properties used in the finite element simulations of a finite-width plate with a central circular hole under uniaxial tension

Parameter	Symbol	Value	Unit
Plate length	L	300	mm
Plate width	w	100	mm
Plate thickness	t	1	mm
Hole diameter ratio	d/w	0.1 – 0.8 (increment 0.1)	-
Elastic modulus	E	200000	MPa
Poisson's ratio	ν	0.3	-
Material [33]	-	ASTM A36 steel	-
Applied Stress	σ	100	MPa

3.2. Finite Element Model, Boundary and Loading Conditions

The finite element model developed for the stress concentration analysis of a finite-width plate with a central circular hole is illustrated in Figure 3. Owing to geometric and loading symmetry, only one half of the plate was modeled to reduce computational cost while preserving accuracy [34]. The global coordinate system adopted in the simulations is also shown in Figure 3, with the x- and y-directions corresponding to the width and loading directions, respectively.

Symmetry boundary conditions were imposed along the vertical centerline of the plate by constraining the horizontal displacement ($U_x = 0$), thereby enforcing deformation compatibility across the plane of symmetry. To prevent rigid-body motion, the bottom edge of the model was restrained in the vertical direction ($U_y = 0$), while remaining in-plane displacements were left unconstrained. A uniform uniaxial tensile stress of $\sigma = 100 \text{ MPa}$ was applied to the top edge of the plate, representing the far-field loading condition.

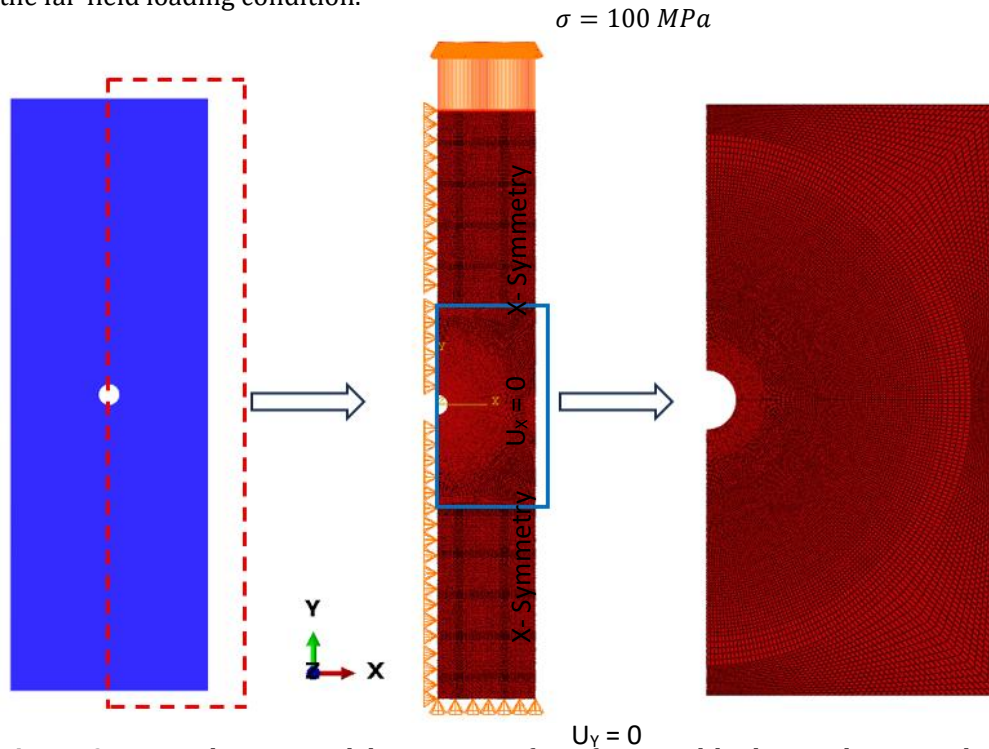


Figure 3. Finite element modeling strategy for a finite-width plate with a central circular hole under uniaxial tension: geometry and symmetry reduction, applied boundary and loading conditions, and locally refined finite element mesh in the vicinity of the hole.

The plate was discretized using two-dimensional plane stress elements appropriate for thin structures. Three quadrilateral element formulations were considered: the fully integrated linear element (CPS4), the reduced-integration element (CPS4R), and the incompatible-mode element (CPS4I) [28]. A progressively refined mesh was employed in the vicinity of the hole boundary, as highlighted in Figure 3, to accurately capture the steep stress gradients associated with stress concentration. The finite element model comprised 30,560 elements and 31,032 corresponding nodes. Mesh quality was carefully controlled through appropriate element sizing and distribution, resulting in an average aspect ratio of 1.57, which is well within the acceptable range for reliable stress predictions. To ensure that the numerical results were independent of mesh density, a systematic mesh convergence study was performed, with particular attention given to the region surrounding the circular hole, where steep stress gradients are known to develop under tensile loading. The mesh was progressively refined by locally increasing the element density along the hole boundary, while a structured and relatively coarser mesh was retained in regions away from the stress concentration zone. The convergence study indicated that further mesh refinement produced only marginal variations in the maximum stress values. Accordingly, the adopted mesh was considered sufficiently refined to accurately capture the stress concentration behavior, while maintaining an efficient balance between numerical accuracy and computational cost. As a result, a mesh convergence study confirmed that computed stress values became independent of element size, plateauing below $\sim 2 \text{ mm}$, as shown in Figure 4. Accordingly, an element size of 1.57 mm was selected to capture the stress concentration accurately and efficiently. Thus, the stress results extracted at the hole edge were subsequently used to evaluate the corresponding stress concentration factors for different hole diameter-to-width ratios, as discussed in the following sections.

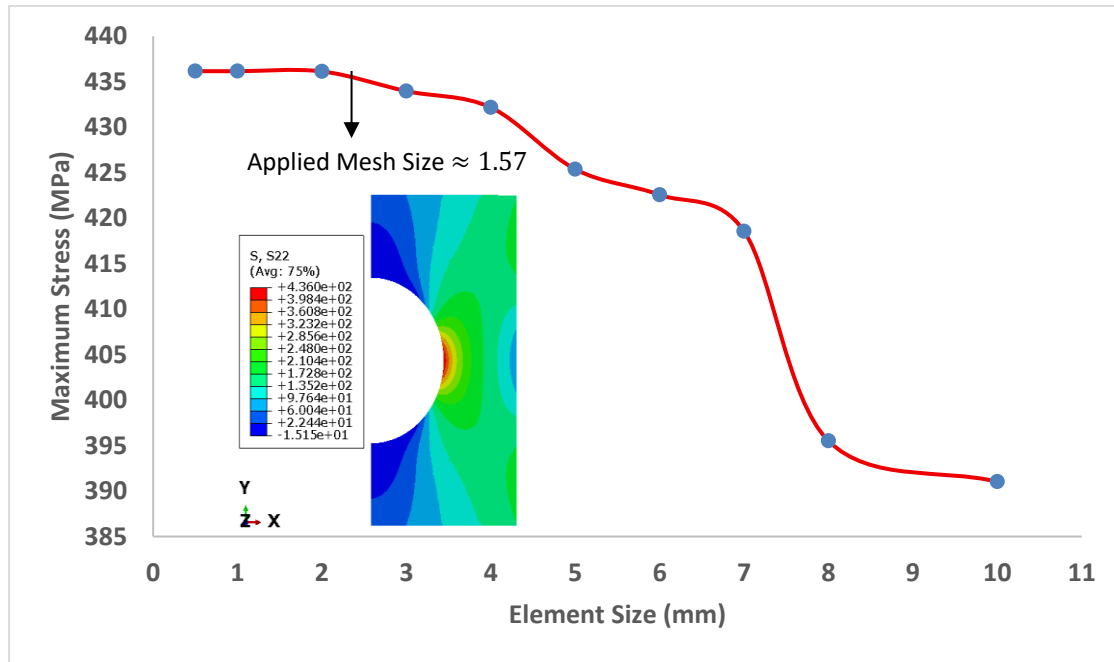


Figure 4. Mesh convergence analysis for a finite-width rectangular plate with a central circular hole ($d/W = 0.5$) under uniaxial tension using CPS4 elements.

3.3. Element Types

The stress analysis of rectangular plates with a central circular hole subjected to uniaxial tensile loading was performed using four-node plane stress elements available in Abaqus, namely CPS4, CPS4R, and CPS4I. These elements are suitable for modeling thin plates, where out-of-plane stresses are negligible and the stress state can be reasonably approximated as plane stress. Under plane stress conditions, the stress component normal to the plate mid-surface and the associated shear stresses vanish, i.e., [35,36].

$$\sigma_z = \tau_{xz} = \tau_{yz} = 0 \quad (9)$$

In this case, the in-plane stresses σ_x , σ_y , and τ_{xy} remain nonzero.

For an isotropic, linear elastic material subjected to plane stress, the constitutive relationship between stresses and strains can be expressed in matrix form as [37]

$$\begin{Bmatrix} \sigma_x \\ \sigma_y \\ \tau_{xy} \end{Bmatrix} = \frac{E}{1-\nu^2} \begin{bmatrix} 1 & \nu & 0 \\ \nu & 1 & 0 \\ 0 & 0 & \frac{1-\nu}{2} \end{bmatrix} \begin{Bmatrix} \varepsilon_x \\ \varepsilon_y \\ \gamma_{xy} \end{Bmatrix} \quad (10)$$

The constitutive relation defined by Eq. (10) corresponds to the plane stress formulation for an isotropic, linear elastic material, in which the in-plane stress components σ_x and σ_y represent the normal stresses acting along the x- and y-directions respectively, while τ_{xy} denotes the in-plane shear stress. These stresses are related to the corresponding strain components, namely the normal strains ε_x and ε_y , and the engineering shear strain γ_{xy} . In this formulation, E is Young's modulus, characterizing the axial stiffness of the material, and ν is Poisson's ratio, which governs the coupling between longitudinal and transverse deformations. The scaling factor $\frac{E}{1-\nu^2}$ arises from the plane stress assumption, under which the out-of-plane stress component σ_z is taken as zero, leading to an effective in-plane stiffness that incorporates Poisson's effect. The off-diagonal terms of the constitutive matrix

reflect the mutual influence of normal strains in orthogonal directions, whereas the shear term, proportional to $\frac{1-\nu}{2}$, represents the material's resistance to in-plane shear deformation [37].

Figure 5 illustrates the four-node plane stress element types adopted in this study, namely CPS4, CPS4R, and CPS4I, along with their associated integration schemes. The CPS4 element is a bilinear quadrilateral plane stress element employing full 2×2 Gauss integration with two in-plane translational degrees of freedom per node [28]. Under uniaxial tensile loading, CPS4 provides stable and accurate stress predictions for well-shaped meshes and is capable of resolving stress concentrations effectively when sufficient mesh refinement is applied in the vicinity of the hole, where stress gradients are most pronounced.

The CPS4R element, also shown in Figure 5, is formulated with reduced integration using a single Gauss point [28]. This approach improves computational efficiency while maintaining adequate accuracy for tensile loading problems. Although reduced integration may introduce hourglass modes, careful control of mesh quality and element aspect ratio in the present study ensured numerical stability, allowing CPS4R to accurately capture both the global tensile stress distribution and the local stress concentration around the hole.

As illustrated in Figure 5, the CPS4I element incorporates incompatible deformation modes into the standard four-node plane stress formulation [28]. These additional internal modes enhance the element's ability to represent in-plane deformation fields and improve stress resolution in regions with steep stress gradients [28]. For the tensile loading case considered, CPS4I yielded a smoother stress distribution and more accurate prediction of peak stresses around the hole boundary, making it particularly effective for stress concentration analysis.

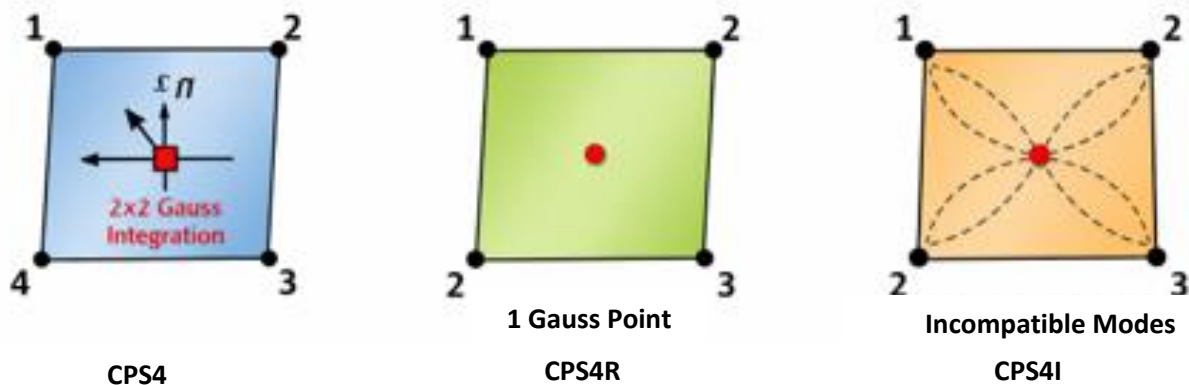


Figure 5. Plane stress element types employed in the simulations [28].

Within each four-node plane stress element (CPS4, CPS4R, and CPS4I), the displacement field is approximated using bilinear shape functions [38]:

$$\mathbf{u}(x, y) = \begin{Bmatrix} u(x, y) \\ v(x, y) \end{Bmatrix} = \sum_{i=1}^4 N_i(x, y) \begin{Bmatrix} u_i \\ v_i \end{Bmatrix} \quad (11)$$

where N_i are the shape functions and u_i, v_i are the nodal displacements in the x- and y-directions, respectively.

The strain field is therefore obtained through the displacement-strain relationship, as follows [38]:

$$\varepsilon = Bd \quad (12)$$

where B is the strain–displacement matrix and d is the vector of nodal displacements. The stress field is then described as [38]

$$\sigma = D\varepsilon \quad (13)$$

Herein, D represents the plane stress constitutive matrix.

Thus, the stiffness matrix of each element in Figure 3 is determined from [38].

$$K_e = \int_{\Omega_e} B^T DB d\Omega \quad (14)$$

where Ω_e represents the element domain. Numerical integration is performed using Gauss quadrature. CPS4 employs full (2×2) integration, CPS4R uses reduced (1-point) integration, and CPS4I incorporates incompatible deformation modes to enhance bending performance while retaining full integration. These formulation differences influence the accuracy and convergence behavior of the stress field, particularly in regions with steep stress gradients such as the vicinity of the circular hole.

3.4. FEM Validation

To establish the reliability and accuracy of the present finite element (FE) framework, a verification study was conducted using a well-documented benchmark problem from the literature involving a finite-width rectangular plate with a central circular hole subjected to uniaxial tension. The reference configuration consists of a rectangular plate with a width of 25 mm, a length of 75 mm, and a thickness of 2 mm [39]. A centrally located circular hole with a radius of 4 mm is introduced, corresponding to a diameter-to-width ratio of $d/w = 0.32$ [39]. The material is defined as DC04 steel with a Young's modulus of 205000 MPa and a Poisson's ratio of 0.3 [39]. A uniform uniaxial tensile stress of 4 MPa is applied to the plate [39].

In the present study, the same geometric configuration, material properties, and loading conditions were replicated. Furthermore, to ensure a consistent basis for comparison, the identical finite element model (Figure 3) and mesh discretization (Figure 4) were adopted. The analysis was performed using the CPS4 element type

The comparison focuses on the equivalent (von Mises) stress distribution and, in particular, the maximum stress concentration occurring around the hole boundary. As shown in Figure 6, the literature reports a maximum equivalent stress of 12.66 MPa [39], whereas the present FE model predicts a value of 12.84 MPa. This corresponds to a deviation of approximately 1.42 percent, indicating excellent agreement.

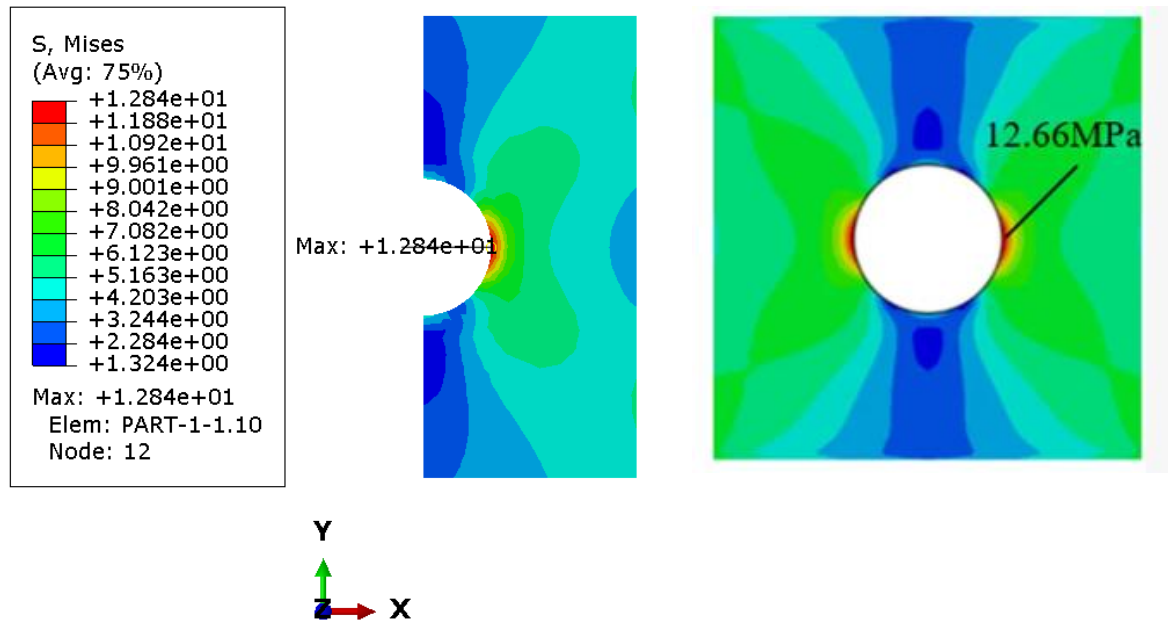


Figure 6. Comparison of equivalent (von Mises) stress distributions around the central hole: (a) present study, and (b) literature results [39].

In addition to the quantitative comparison, the contour plots of the equivalent stress distribution shown in Figure 6 demonstrate a high degree of consistency with the reference solution, particularly in capturing the stress concentration pattern and gradient around the hole. This close correlation confirms that the adopted modeling strategy, including element selection, mesh density, and boundary conditions, is capable of accurately reproducing the mechanical response of the problem. Overall, the strong agreement between the present results and the literature validates the robustness and accuracy of the developed finite element model, thereby providing confidence in its subsequent application to the parametric investigations presented in this study.

4. Results and Discussion

4.1. Theoretical Results

Table 2 summarizes the geometric stress concentration factor K_{tg} obtained from Eq. (2) and the corresponding maximum stresses σ_{max} calculated using Eq. (3) for different hole diameter-to-width (d/w) ratios. Eq. (2) defines K_{tg} as a function of d/w , while Eq. (3) relates the maximum stress to the applied nominal stress through $\sigma_{max} = K_{tg}\sigma$. The variation of σ_{max} with respect to d/w is illustrated in Figure 7, providing a clear representation of the geometric amplification effect under uniaxial tensile loading. As shown in Table 2 and Figure 7, a nonlinear relationship exists between d/w and both K_{tg} and σ_{max} . For small hole sizes ($d/w = 0.1$), the stress concentration factor is 3.035, corresponding to a maximum stress of 303.5 MPa. In this range, the plate behaves similarly to an infinite plate, where the theoretical stress concentration factor is approximately 3 [40]. As d/w increases to 0.3–0.4, only a moderate rise in K_{tg} is observed, indicating that the ligament width remains sufficient to redistribute stresses. However, beyond $d/w = 0.5$, both K_{tg} and σ_{max} increase rapidly. At $d/w = 0.6$, the maximum stress exceeds 500 MPa, which is more than five times the applied nominal stress ($\sigma = 100$ MPa). When d/w reaches 0.8, K_{tg} increases to 10.216, resulting in a maximum stress of 1021.6 MPa—over ten times the applied stress. This sharp increase highlights the strong sensitivity of stress concentration to the reduction in ligament width. As illustrated in Figure 7, the curve steepens significantly at higher d/w ratios, reflecting the accelerated growth of stress concentration. This behavior is attributed to the progressive reduction of the effective load-carrying ligament, which forces the applied load to pass through a diminishing cross-sectional area. Consequently, stress gradients intensify near the hole boundary, and stress concentration becomes dominant. As the hole size

approaches the plate width $d/w \rightarrow 1$, the ligament width tends to zero and K_{tg} approaches infinity, indicating the loss of load-carrying capacity [31]. This asymptotic trend explains the pronounced nonlinearity observed in Table 2 and Figure 7.

For d/w values beyond approximately 0.8, the physical interpretation of K_{tg} becomes increasingly critical. In this regime, the remaining ligament is extremely narrow, and the stress field transitions from distributed to highly localized. Small increases in hole size result in disproportionately large increases in stress, indicating that the structure is approaching a geometric instability condition. Here, K_{tg} no longer serves solely as a geometric amplification factor but also reflects the degradation of the load-transfer mechanism.

From a design perspective, such high K_{tg} values have limited practical relevance, as material yielding or fracture would likely occur before these extreme stresses are reached. Thus, for $d/w > 0.8$, K_{tg} should be interpreted as an indicator of imminent structural failure rather than a purely theoretical parameter. This behavior underscores the inherent limitation of perforated plates under tensile loading: as the ligament width decreases, structural integrity deteriorates rapidly in a highly nonlinear manner [31].

Table 2. Variation of the geometric stress concentration factor K_{tg} and the corresponding maximum stress σ_{max} for different hole diameter-to-width ratios (d/w) under uniaxial tension.

d/w	K_{tg} (Eq. 2)	σ , (MPa) Applied Stress	$\sigma_{max} = K_{tg} \cdot \sigma$ (Eq. 3)
0.1	3.035	100	303.5
0.2	3.148	100	314.8
0.3	3.367	100	336.7
0.4	3.732	100	373.2
0.5	4.314	100	431.4
0.6	5.255	100	525.5
0.7	6.889	100	688.9
0.8	10.216	100	1021.6

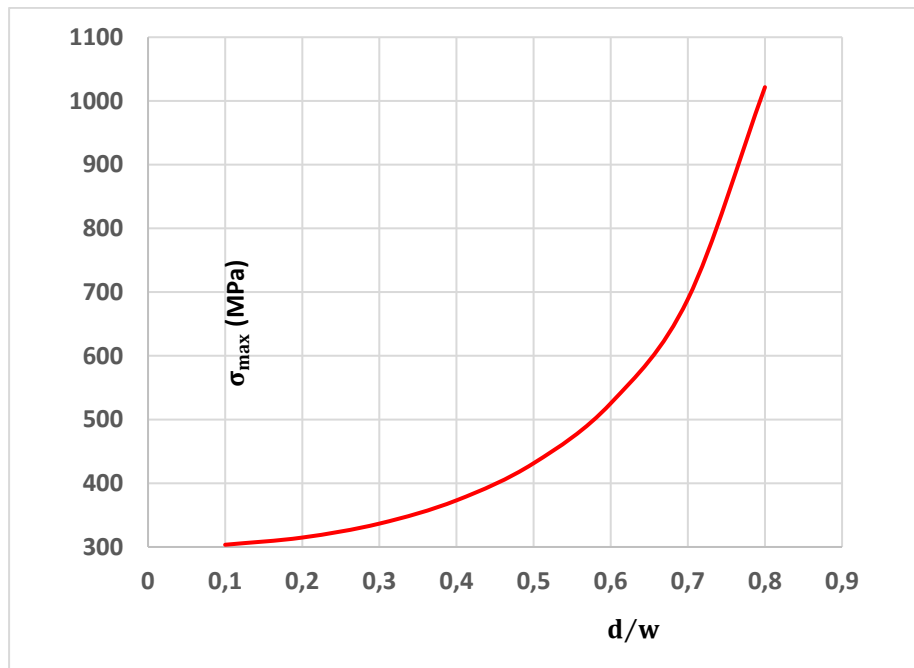


Figure 7. Variation of the maximum stress σ_{max} with d/w ratio for a finite-width rectangular plate with a central circular hole under uniaxial tension.

It should be noted that, although the maximum stress values in this study were evaluated using the gross-section-based stress concentration factor K_{tg} , the expressions provided in Eqs. (4) – (8) offer an alternative and theoretically consistent framework for determining σ_{max} . This formulation, based on the net-section stress concentration factor K_{tn} , enables the separation of net-section stress amplification from the geometric disturbance caused by the hole [31]. Accordingly, the maximum stress can equivalently be calculated using K_{tn} together with the corresponding relationships. This approach is particularly useful when the objective is to isolate the geometric contribution to stress concentration independently of the reduction in effective load-carrying area. Such a distinction is especially important in advanced analyses involving local yielding, crack initiation, damage evolution, and sensitivity to stress gradients.

By adopting the K_{tn} -based framework, a clearer physical interpretation of stress concentration phenomena can be achieved, allowing for more accurate assessment of local failure mechanisms in perforated structural components subjected to tensile loading [31].

4.2. Finite Element Analysis Results

The S_{22} (σ_y) stress contour distributions obtained from CPS4, CPS4R, and CPS4I plane stress elements are presented for various hole diameter-to-width ratios (d/w) under uniaxial tension in Figure 8. The comparison is carried out strictly among the element formulations, with emphasis on the consistency of stress patterns, the resolution of stress gradients, and the characteristics of stress localization around the hole boundary.

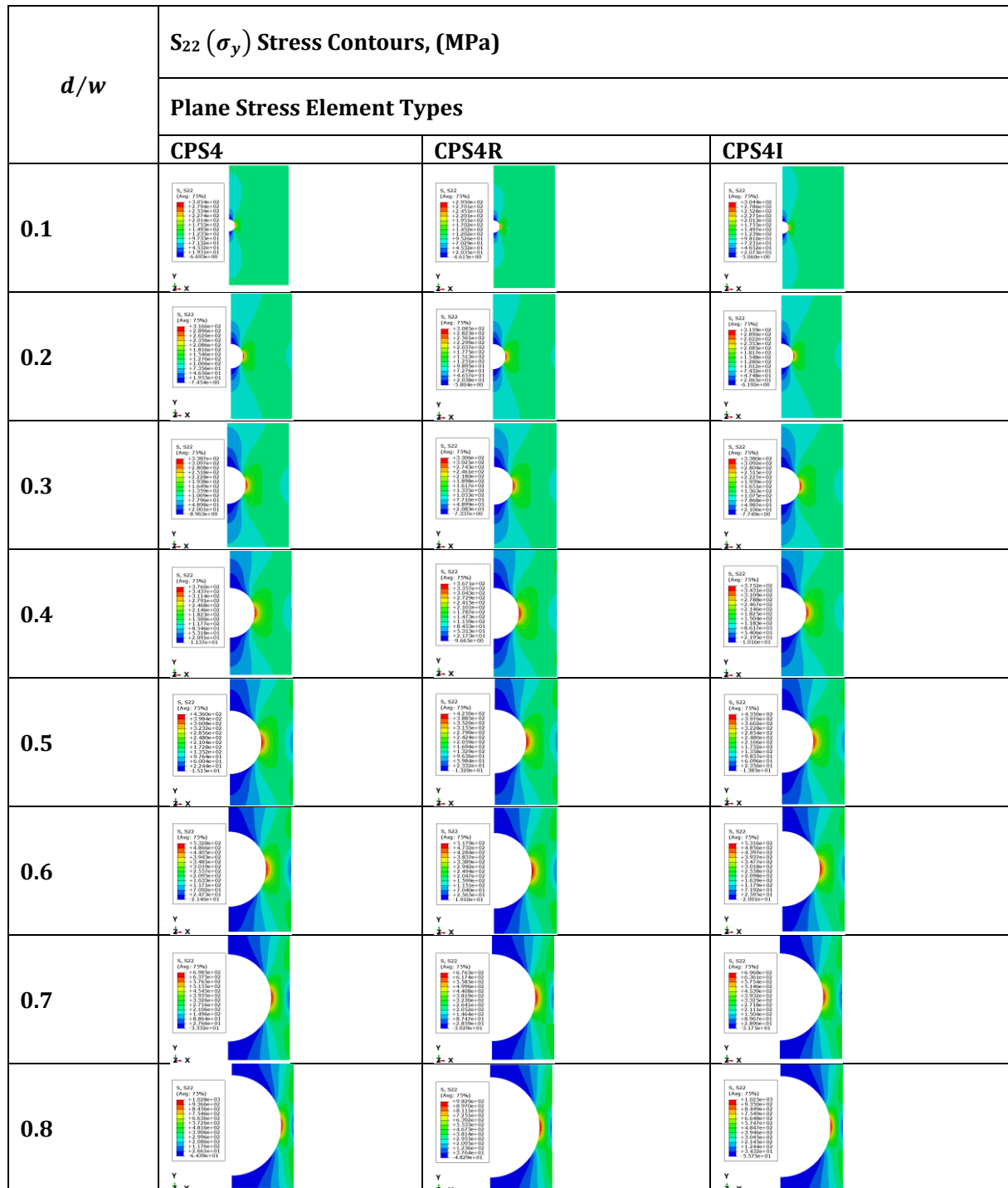


Figure 8. Comparison of $S_{22} (\sigma_y)$ stress distributions obtained using different plane stress element types (CPS4, CPS4R, and CPS4I) for various hole diameter-to-width ratios (d/w) under uniaxial tension.

As shown in Figure 8, for small hole ratios ($d/w = 0.1 - 0.2$), all three element types produce nearly identical stress contour patterns. The stress field is smooth and symmetric, with moderate amplification around the hole boundary and a gradual transition to the far-field tensile stress. No contour distortion, spurious oscillation, or numerical instability is observed. This strong agreement indicates that when stress gradients are mild, the choice of integration scheme or incompatible mode enhancement has a negligible effect on both global and local stress representation.

As the hole ratio increases to intermediate values ($d/w = 0.3 - 0.5$), stress gradients near the hole edge become steeper due to ligament reduction. Under these conditions, subtle differences begin to emerge. CPS4 and CPS4R continue to exhibit similar contour patterns with comparable localization zones, whereas CPS4I shows slightly smoother transitions in the high-stress region adjacent to the hole boundary, reflecting its improved representation of in-plane stress variation. Despite these differences, the overall stress distribution, symmetry, and peak stress locations remain consistent across all formulations.

For larger ratios ($d/w \geq 0.6$), where the ligament becomes narrow and stress localization intensifies, accurate representation of steep gradients becomes more critical. CPS4 maintains stable and symmetric contours, although the high-stress band appears slightly sharper. CPS4R produces similar global patterns without visible hourglass-induced irregularities, indicating that mesh refinement effectively mitigates reduced integration effects. CPS4I yields comparatively smoother and more uniform stress transitions in the critical ligament region, particularly at $d/w = 0.7$ and 0.8 . Nevertheless, the qualitative stress flow and peak stress locations remain identical for all element types.

Following this qualitative assessment, the maximum stress values reported in Table 3 provide further insight into the quantitative influence of element formulation. The results reveal a clear and consistent trend across all d/w ratios. CPS4 and CPS4I produce nearly identical maximum stresses throughout the entire range, with differences generally within 1%, even at large hole ratios. For example, at $d/w = 0.8$, CPS4 predicts 1028 MPa, while CPS4I yields 1025 MPa, indicating virtually identical performance in capturing stress concentration severity. This agreement confirms that both formulations effectively resolve steep stress gradients in the present problem.

In contrast, CPS4R consistently predicts slightly lower peak stresses. While the difference is small at low d/w ratios, it becomes more pronounced as d/w increases. At $d/w = 0.1$, CPS4R predicts 295 MPa compared to 305.4 MPa for CPS4, and at $d/w = 0.8$, it yields 982.9 MPa versus 1028 MPa. This systematic reduction suggests a marginally softer numerical response associated with reduced integration in regions of high stress gradients. Despite these differences, the relative ranking of the element types remains consistent across all cases ($CPS4 > CPS4I > CPS4R$).

In summary, all three formulations produce mechanically consistent and symmetric stress distributions. CPS4 and CPS4I demonstrate nearly identical capability in predicting peak stresses, whereas CPS4R tends to slightly underestimate stress concentration intensity. The influence of element formulation becomes more pronounced as geometric discontinuity increases, particularly when accurate evaluation of maximum stress is critical for local failure or damage initiation analyses. A detailed assessment of prediction accuracy is provided in the subsequent section through comparison with theoretical results.

Table 3. Comparison of predicted maximum S_{22} (σ_y) stresses at the hole boundary obtained using CPS4, CPS4R, and CPS4I plane stress elements for various hole diameter-to-width ratios (d/w) under uniaxial tension.

d/w	Predicted Maximum Stress (σ_{max}) (MPa)		
	CPS4	CPS4R	CPS4I
0.1	305.4	295	304.4
0.2	316.6	308.5	315.9
0.3	338.7	330.6	338
0.4	376	367.1	375.2
0.5	436	425	435
0.6	532.8	517.9	531.6
0.7	698.5	676.3	696.8
0.8	1028	982.9	1025

4.3. Comparison (Theory vs. FEM)

Table 4 compares the theoretical maximum stresses with the finite element predictions obtained using CPS4, CPS4R, and CPS4I elements for various hole diameter-to-width (d/w) ratios. The corresponding error ratios are also presented in Table 4 and graphically illustrated in Figure 9 to better highlight the performance trends of the element formulations.

As observed, the theoretical maximum stress (σ_{max}) increases markedly with increasing d/w , rising from 303.5 MPa at $d/w = 0.1$ to 1021.6 MPa at $d/w = 0.8$. This pronounced increase is attributed to the intensified stress concentration effect associated with larger hole diameters relative to the plate width [31,41]. All finite element models successfully capture this trend, demonstrating their ability to represent the global stress concentration behavior. Despite this overall agreement, differences in accuracy are evident among the element types. The CPS4 element consistently overestimates the maximum stress compared to the theoretical solution, with positive error ratios ranging from 0.571% to 1.393% for $0.1 \leq d/w < 0.7$. At $d/w = 0.8$, the error slightly decreases to 0.626%. The gradual increase in error up to $d/w = 0.7$ suggests that, as stress gradients become steeper, the fully integrated CPS4 element tends to produce slightly stiffer responses, leading to an overprediction of peak stresses.

In contrast, the CPS4R element systematically underestimates the theoretical stress values across all d/w ratios, as evident in both Table 4 and Figure 9. The error ratios range from -1.446% to -3.788%, with the largest deviation occurring at $d/w = 0.8$. This consistent negative error trend indicates a softer numerical response, which can be attributed to reduced integration effects. While reduced integration enhances computational efficiency, it may lead to a slight underestimation of stress concentrations in regions with high stress gradients, particularly for larger hole sizes.

Table 4. Comparison of theoretical and finite element maximum stresses and corresponding error ratios for different element types at various hole diameter-to-width (d/w) ratios.

d/w	Maximum Stress (σ_{max}) (MPa)				Error Ratio %					
	Theory	FEM			$[(\sigma_{FEM} - \sigma_{Theory})/\sigma_{Theory}] \times 100$					
		CPS4	CPS4R	CPS4I	Theory vs. Theory CPS4	vs. Theory CPS4R	vs. Theory CPS4I	vs. Theory CPS4I	vs. Theory CPS4I	vs. Theory CPS4I
0.1	303.5	305.4	295	304.4	0.626	-2.800	0.296			
0.2	314.8	316.6	308.5	315.9	0.571	-2.001	0.349			
0.3	336.7	338.7	330.6	338	0.594	-1.811	0.386			
0.4	373.2	376	367.1	375.2	0.750	-1.634	0.535			
0.5	431.4	436	425	435	1.066	-1.483	0.834			
0.6	525.5	532.8	517.9	531.6	1.389	-1.446	1.160			
0.7	688.9	698.5	676.3	696.8	1.393	-1.829	1.146			
0.8	1021.6	1028	982.9	1025	0.626	-3.788	0.332			

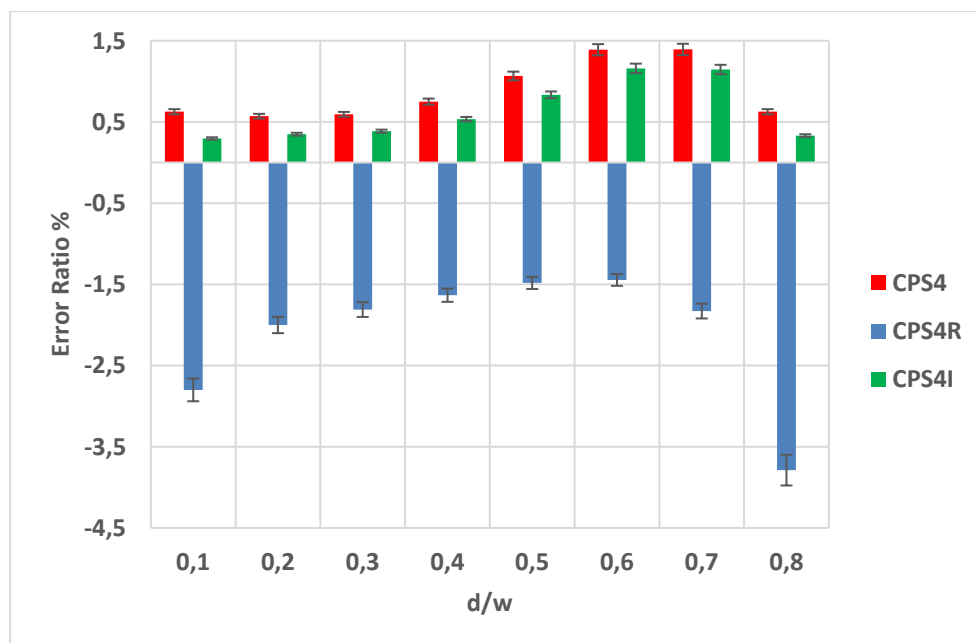


Figure 9. Comparison of error ratios (%) for CPS4, CPS4R, and CPS4I elements relative to theoretical maximum stress values across varying d/w ratios.

As shown in Table 4 and Figure 9, the CPS4I element exhibits the most balanced and reliable performance among the three formulations. Its error ratios remain consistently small and positive, ranging from 0.296% to 1.160%, indicating excellent agreement with the theoretical predictions across the entire range of d/w ratios. Compared to CPS4, CPS4I generally yields lower deviations, particularly at small and moderate d/w ratios where accurate representation of stress gradients is critical. The results also demonstrate a smooth and stable trend without abrupt fluctuations. Even at the highest geometric severity ($d/w = 0.8$), the deviation remains limited to 0.332%, confirming its strong predictive capability under pronounced stress concentration conditions. This improved

performance can be attributed to the incompatible mode enhancement, which refines the strain field representation and enables a more accurate capture of localized stresses. In contrast to the systematic overestimation observed in CPS4 and the underestimation associated with CPS4R, CPS4I maintains both numerical stability and accuracy across all cases considered. This consistent behavior highlights its suitability for stress concentration analyses, where reliable prediction of peak stresses is essential.

From a comparative standpoint, although all element types provide acceptable accuracy within a relatively narrow error band (approximately within $\pm 4\%$), clear differences emerge in terms of consistency and predictive reliability. Among the three formulations, CPS4I demonstrates the most stable and systematic agreement with the theoretical solutions across the entire d/w range. Its deviations remain small, uniformly distributed, and do not exhibit abrupt increases, even at high geometric severity, indicating a strong capability to capture steep stress gradients associated with pronounced stress concentrations. While CPS4 produces moderate overestimations within acceptable engineering tolerances, and CPS4R exhibits comparatively larger underestimations—particularly at higher d/w ratios—the CPS4I element maintains both numerical robustness and high fidelity to the theoretical response. This balanced performance is especially important in stress concentration analyses, where even small inaccuracies in peak stress prediction can significantly influence design safety margins and failure assessments.

In addition to the comparison based on peak stress values (Table 4), the performance of the considered element formulations was further evaluated in terms of mesh sensitivity, numerical stability, stress gradient resolution, and computational efficiency. A uniform mesh density was employed for all element types to ensure a consistent basis for comparison, thereby isolating the influence of element formulation on the predicted response. The mesh size was selected through a convergence study using the CPS4 element, providing a stable reference solution. Within this framework, CPS4I demonstrates reduced mesh sensitivity by delivering accurate stress predictions without the need for excessive refinement, whereas CPS4 and particularly CPS4R exhibit greater dependence on mesh density to achieve comparable accuracy. From a numerical stability standpoint, CPS4 maintains robust behavior due to full integration, while CPS4R, although computationally efficient, may be prone to reduced accuracy associated with its integration scheme. In contrast, CPS4I provides a stable and consistent response owing to its enhanced kinematic representation. The ability to resolve steep stress gradients near the hole boundary is most effectively captured by CPS4I, highlighting its superiority in representing localized stress fields, whereas CPS4 and CPS4R tend to underestimate peak stresses unless finer meshes are adopted. In terms of computational efficiency, CPS4R offers lower computational cost, while CPS4I achieves an improved balance between accuracy and efficiency by reducing the need for mesh refinement. Overall, these observations emphasize that element formulation plays a critical role in accurately capturing stress concentration phenomena.

Furthermore, the observed differences in stress predictions (Table 4 and Figure 9) among the element formulations can be attributed to their underlying numerical characteristics, particularly the integration schemes and strain field representations [28]. The CPS4 element, based on full integration, provides stable results but has limited capability in capturing steep stress gradients with coarse meshes [28]. This limitation arises because the bilinear displacement interpolation leads to a constant strain field within each element, restricting its ability to accurately represent rapidly varying stress fields near geometric discontinuities. The CPS4R element, using reduced integration, improves computational efficiency but may underestimate peak stresses due to less accurate strain field sampling. In addition, the use of a single integration point can result in an overly compliant stiffness response and may introduce spurious deformation modes, which further reduces its accuracy in regions with high stress gradients. In contrast, the CPS4I element incorporates incompatible modes, enriching the displacement field and enabling a more accurate representation of localized deformation [28]. These additional internal degrees of freedom enhance the element's ability to capture bending-dominated and highly non-uniform strain states without requiring mesh refinement. This allows CPS4I to better capture stress concentrations near the hole, where steep gradients dominate the response. Consequently, CPS4I provides a more realistic stiffness representation and improved stress recovery, particularly in regions where stress gradients are severe and conventional displacement-based

elements exhibit limitations.

Therefore, for the analysis of perforated plates subjected to increasing geometric severity, the CPS4I element stands out as the most reliable and technically sound choice. Its enhanced strain field representation not only improves local stress prediction but also ensures consistent performance over a wide range of configurations, underscoring its importance for accurate and dependable finite element modeling of stress concentration problems.

5. Concluding Remarks

This study evaluated the performance of CPS4, CPS4R, and CPS4I plane stress elements in predicting stress concentration in perforated plates over a range of hole diameter-to-width d/w ratios. Numerical results were compared with theoretical stress concentration factors, namely the gross-section factor K_{tg} and the net-section factor K_{tn} , providing a consistent benchmark for assessing element accuracy.

All element types successfully reproduced the increasing trend of maximum stress and corresponding stress concentration factors with increasing d/w , confirming their ability to capture the global response. However, systematic differences were observed in the prediction of peak stresses. CPS4 showed slight overestimation, whereas CPS4R consistently underestimated the theoretical values, with deviations becoming more pronounced at higher d/w ratios where stress gradients intensify.

The CPS4I element demonstrated the most consistent and reliable agreement with K_{tg} based maximum stress solutions across the entire investigated range. Its error levels remained small and stable, even at $d/w = 0.8$, indicating superior capability in resolving localized stress concentrations due to its enhanced strain field formulation. This robustness makes CPS4I particularly suitable for analyses where accurate peak stress prediction is critical for design and safety assessment.

It should be noted that for $d/w > 0.8$, the stress concentration behavior becomes increasingly questionable from a theoretical standpoint. At such high ratios, the remaining ligament width is significantly reduced, and the assumptions underlying classical closed-form solutions for K_{tg} and K_{tn} may no longer be fully valid. Consequently, predictions in this range should be interpreted with caution, as both theoretical and numerical results may be affected by limitations in applicability and increased sensitivity to modeling assumptions.

However, the limitations of the present study should be underlined: it considers a single material (ASTM A36 steel, $\nu = 0.3$) and a fixed load magnitude ($\sigma = 100 \text{ MPa}$). The stress concentration factors employed are based on Peterson's empirical formulations [31], which are valid for isotropic, linear-elastic, ductile metals; therefore, caution should be exercised when extending the findings to materials with different elastic properties, non-metallic behavior, or significant plasticity. Variations in material class, Poisson's ratio, or element aspect ratios may influence stress magnitudes, convergence behavior, and the relative performance of the element formulations. Future investigations could systematically explore these factors, along with a wider range of loading conditions, to evaluate the robustness and generality of the present results across diverse materials and structural configurations.

In summary, while all examined elements provide acceptable accuracy within the validated range, CPS4I offers the most robust and dependable performance for stress concentration analysis of perforated plates, particularly under increasing geometric severity.



Peer-review: External, Independent.

Acknowledgements:

-

Declarations:

1. Statement of Originality:

This work is original.

2. Author Contributions:

Concept: MAD,OÖ; **Conceptualization:** MAD,OÖ; **Literature Search:** MAD,OÖ,KE; **Data Collection:** OÖ,KE; **Data Processing:** MAD,KE; **Analysis:** MAD,KE; **Writing – original draft:** MAD,OÖ; **Writing – review & editing:** MAD,OÖ.

3. Ethics approval:

Not applicable.

4. Funding/Support:

This work has not received any funding or support.

5. Competing Interests:

The authors declare no competing interests.

6. GenAI Usage Statement:

No GenAI tools were used at any stage of the study.

7. Sustainable Development Goals:



REFERENCES

- [1] Maiorana E, Pellegrino C, Modena C. Elastic stability of plates with circular and rectangular holes subjected to axial compression and bending moment. *Thin-Walled Structures* 2009;47:241–55. <https://doi.org/10.1016/j.tws.2008.08.003>.
- [2] J BC, L YA, Mark B. Stability of Plates with Rectangular Holes. *Journal of Structural Engineering* 1987;113:1111–6. [https://doi.org/10.1061/\(ASCE\)0733-9445\(1987\)113:5\(1111\)](https://doi.org/10.1061/(ASCE)0733-9445(1987)113:5(1111)).
- [3] Thang NN, Vinh NT, Van Son N, Duong LT. Investigation of Stress-Field Evolution and Stress Concentration in Plates Using the Vector Form Intrinsic Finite Element (VFIFE) Method. *Iranian Journal of Science and Technology, Transactions of Mechanical Engineering* 2026. <https://doi.org/10.1007/s40997-025-00951-6>.
- [4] Pilkey WD, Pilkey DF, Bi Z. *Peterson’s stress concentration factors*. John Wiley & Sons; 2020.
- [5] Meyers MA, Chawla KK. *Mechanical behavior of materials*. Cambridge university press; 2008.
- [6] Peterson RE. *Stress concentration factors: Charts and relations useful in making strength calculations for machine parts and structural elements(Book)*. New York, Wiley-Interscience, 1974 329 p 1974.
- [7] Gross D, Hauger W, Schröder J, Wall WA, Bonet J. *Engineering mechanics 2*. Springer; 2011.
- [8] Young WC, Budynas RG, Sadegh AM. *Roark’s formulas for stress and strain. vol. 7*. McGraw-hill New York; 2002.
- [9] Kirsch EG. Die Theorie der Elastizität und die Bedürfnisse der Festigkeitslehre. *Zeitschrift Des Vereines Deutscher Ingenieure* 1898;42:797–807.

- [10] Savin GN. Stress concentration around holes. (No Title) 1961.
- [11] Lekhnitskii SG. Anisotropic plates, gordon and breach. Science Publ 1968.
- [12] Goodier SPTJN. Theory of elasticity McGraw-Hill New York 1970.
- [13] Patel RH, Patel BP. Effect of various discontinuities present in a plate on stress concentration: a review. *Engineering Research Express* 2022;4:032001. <https://doi.org/10.1088/2631-8695/ac8c1b>.
- [14] Gunwant D, Singh JP. Stress and displacement analysis of a rectangular plate with central elliptical hole. *International Journal of Engineering and Innovative Technology* 2013;3:387–92.
- [15] Nikolić V, Dolićanin Ć, Radojković M. Application of finite element analysis of thin steel plate with holes. *Tehnički Vjesnik* 2011;18:57–62.
- [16] Zienkiewicz OC, Taylor RL. The finite element method set. Elsevier; 2005.
- [17] Belytschko T, Liu WK, Moran B, Elkhodary K. Nonlinear finite elements for continua and structures. John wiley & sons; 2014.
- [18] Zienkiewicz OC, Taylor RL. The finite element method for solid and structural mechanics. Elsevier; 2005.
- [19] Bathe K-J. Finite element procedures prentice-hall. New Jersey 1996;1037:1–6.
- [20] Pan Z, Cheng Y, Liu J. Stress analysis of a finite plate with a rectangular hole subjected to uniaxial tension using modified stress functions. *Int J Mech Sci* 2013;75:265–77. <https://doi.org/10.1016/j.ijmecsci.2013.06.014>.
- [21] Systèmes D. ABAQUS Documentation (Dassault Systèmes, Providence, RI) 2014.
- [22] Kawecki B, Podgórski J. Numerical results quality in dependence on Abaqus plane stress elements type in big displacements compression test. *Applied Computer Science* 2017;13:56–64. <https://doi.org/10.23743/acs-2017-29>.
- [23] Mahmud J, Holt C, Evans S, Manan NFA, Chizari M. A Parametric Study and Simulations in Quantifying Human Skin Hyperelastic Parameters. *Procedia Eng* 2012;41:1580–6. <https://doi.org/10.1016/j.proeng.2012.07.353>.
- [24] Cen S, Zhou P-L, Li C-F, Wu C-J. An unsymmetric 4-node, 8-DOF plane membrane element perfectly breaking through MacNeal’s theorem. *Int J Numer Methods Eng* 2015;103:469–500. <https://doi.org/10.1002/nme.4899>.
- [25] Simo JC, Rifai MS. A class of mixed assumed strain methods and the method of incompatible modes. *Int J Numer Methods Eng* 1990;29:1595–638. <https://doi.org/10.1002/nme.1620290802>.
- [26] Sun EQ. Shear locking and hourglassing in MSC Nastran, ABAQUS, and ANSYS. Msc software users meeting, 2006, p. 1–9.
- [27] Cook RD. Concepts and applications of finite element analysis. John wiley & sons; 2007.
- [28] Systèmes D. Abaqus Analysis User’s Manual: Element Library. Dassault Systèmes 2016.
- [29] Pilkey WD, Pilkey WD. Formulas for stress, strain, and structural matrices. vol. 107. John Wiley & Sons Hoboken, NJ, USA; 2005.
- [30] Savruk MP, Kazberuk A. Stress concentration at notches. Springer; 2017.
- [31] Pilkey WD, Pilkey DF, Bi Z. Peterson’s stress concentration factors. John Wiley & Sons; 2020.
- [32] Budynas RG, Nisbett JK. Shigley’s mechanical engineering design. vol. 9. McGraw-Hill New York; 2011.

- [33] Bernuzzi C, Cordova B. Structural steel design to Eurocode 3 and AISC specifications. John Wiley & Sons; 2016.
- [34] Bakhshi N, Taheri-Behrooz F. Length effect on the stress concentration factor of a perforated orthotropic composite plate under in-plane loading. *Int J Compos Mater* 2019;1:71–90.
- [35] Ha-Young W, W LA, Jae-Hoon K. Exact Solutions for Stresses, Strains, Displacements, and Stress Concentration Factors of a Perforated Rectangular Plate by a Circular Hole Subjected to In-Plane Bending Moment on Two Opposite Edges. *J Eng Mech* 2014;140:04014023. [https://doi.org/10.1061/\(ASCE\)EM.1943-7889.0000732](https://doi.org/10.1061/(ASCE)EM.1943-7889.0000732).
- [36] Reiss EL, Locke S. On the theory of plane stress. *Q Appl Math* 1961;19:195–203.
- [37] Hibbeler RC, Fan SC. Statics and mechanics of materials. vol. 2. Prentice Hall Singapore; 2004.
- [38] Logan DL. A first course in the finite element method. vol. 4. Thomson; 2011.
- [39] You H, Zhang L, Lin X, Tang P, Du Q. Stress concentration characteristics and coefficient modification for DC04 steel with holes of finite thickness. *Front Mater* 2025;Volume 12-2025. <https://doi.org/10.3389/fmats.2025.1692324>.
- [40] Kirsch EG. Die Theorie der Elastizität und die Bedingungen der Festigkeitslehre. *Zeitschrift Des Vereines Deutscher Ingenieure* 1898;42:797–807.
- [41] Young WC, Budynas RG, Sadegh AM. Roark's formulas for stress and strain. vol. 7. McGraw-hill New York; 2002.

